

УДК 539.234

Spintronics: Magnetism and Spin-Dependent Transport on the Nanometer Scale

Daniel E. Bürgler*

Institute of Solid State Research, Electronic Properties (IFF-9) and
Jülich-Aachen Research Alliance, Fundamentals of Future Information Technology (JARA-FIT),
Research Center Jülich GmbH, D-52425 Jülich,
Germany

Received 22.09.2009, received in revised form 10.01.2010, accepted 30.01.2010

Since the discovery of interlayer exchange coupling and giant magnetoresistance (GMR) in the 1980's spin-dependent transport in magnetic multilayer and nanostructures has attracted a lot of interest. The research was motivated by applications — i.e. GMR read-heads in computer harddisks and the magnetic random access memory (MRAM) — as well as exciting new phenomena, which nowadays constitute the research field called spintronics. The field rapidly developed from investigating magnetic multilayers with layer thicknesses in the nanometer range to a true nanotechnology, which explores magnetism and spin-dependent transport on a nanometer scale. Typical devices are sub-micron sized in all three space dimensions. The recognition of spintronics as a pioneering field for future nanoelectronics culminated in the award of the Nobel Prize in Physics 2007 for the discovery of the GMR effect. Interlayer exchange coupling, giant and tunneling magnetoresistance (GMR, TMR), and current-induced magnetization dynamics as the major novel phenomena of spintronics are reviewed. For each of them a comprehensible physical picture is introduced and discussed.

Keywords: spintronics, interlayer exchange coupling, giant magnetoresistance, tunneling magnetoresistance, spin-transfer torque.

Introduction

In conventional electronic devices the charge of electrons is used to realize certain functionalities by controlling electric currents, e.g. by electric fields. Therefore, conventional electronics bases on charge transport. The spin is a further fundamental property of electrons. The electronic spins correspond to magnetic moments, which give rise to the magnetism of solids. The spin also provides a means to act with spin-dependent influences, e.g. a magnetic field and spin-dependent scattering, on the electrons and their motion. In addition, a spin current can transfer spin momentum between different parts of a system. This gives rise to novel spin-transfer torque concepts for the manipulation of the magnetization in nanoscale magnets. In contrast to the electric charge of an electron, which is always negative and conserved, the spin degree of freedom can adopt two orientations with respect to a given quantization axis, spin-up and spin-down. In a ferromagnetic material, due to the imbalance of the two spin orientations spin transport is associated to an electrical current. In this context, one defines the spin polarization of the current by

$$P = \frac{N^\uparrow - N^\downarrow}{N^\uparrow + N^\downarrow}, \quad (1)$$

*d.buergler@fz-juelich.de

where $N^{\uparrow(\downarrow)}$ is the number of spin-up (spin-down) electrons taking part in the transport. $|P| = 100\%$ indicates a completely polarized current, whereas $P = 0$ corresponds to an unpolarized current with no associated spin transport. Transport effects and electronic devices that take advantage of the spin degree of freedom of the electron to achieve new functionalities constitute the field called spintronics (or magnetoelectronics).

For electrons in a solid state environment, the spin polarization P is in general not conserved. The spin can be flipped for instance by electron-electron interaction or spin-flip scattering from magnetic impurities. The characteristic length scale for spin transport in a solid, within which P is conserved, is the spin diffusion (or spin-flip) length λ defined by

$$P(x) = P_0 \exp\left(-\frac{x}{\lambda}\right), \quad (2)$$

where P_0 is the initial spin polarization at the position $x = 0$. The value of λ is material-dependent and varies in the range from a few nanometers (e.g. $\text{Ni}_{80}\text{Fe}_{20}$ alloy, also called Permalloy) up to several tens of nanometers (e.g. Co) for magnetic alloys and metals and exceeds 100 nm for nonmagnetic metals (e.g. Cu). λ also depends on extrinsic properties like crystallinity and purity of the material. But in most cases – in particular those dealing with elemental metals and their alloys – spin transport only persists over distances of the order of a few nanometers. For this reason layered structures with individual layer thicknesses of the order of a few nanometers play a crucial role for spin transport effects. The interfaces between neighbouring layers additionally give rise to spin-dependent reflection, transmission, and scattering.

The main focus of this review will be on the new effects, namely Interlayer Exchange Coupling (IEC, Sect. 1.), Giant Magnetoresistance (GMR, Sect. 2.), Tunnel Magnetoresistance (TMR, Sect. 3.), and Spin-Transfer Torque effects (STT, Sect. 4.). They have been discovered only during the past 15 years and immediately attracted a lot of interest due to their high potential for applications in spintronics.

1. Interlayer Exchange Coupling (IEC)

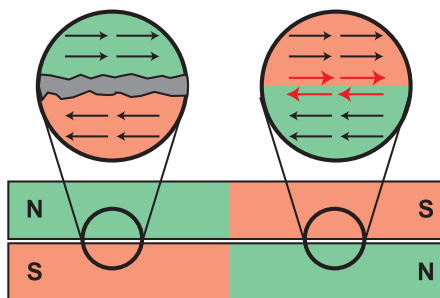


Fig. 1. Two permanent magnets align antiparallel due to their fringing fields. In a real experiment (left inset) the two magnets are separated due to oxides, contamination, and roughness at the surface. For ideal surfaces (right inset) the antiparallel alignment leads to conflicts at the interface as indicated by the red arrows

What happens when two ferromagnets are brought in close proximity? One can try to address this question in a macroscopic experiment with two permanent magnets. They will arrange

themselves in an antiparallel manner because the north pole of the first magnet will attract the south pole of the second and vice versa (Fig. 1). This type of coupling is due to the fringing fields and thus of dipolar nature. The antiparallel alignment minimizes the fringing field energy. However, this macroscopic experiment does not really address the question of interest because an oxide layer, contamination, and roughness prohibit that the ferromagnets come in close proximity, i.e. at a separation of a few Ångströms, where direct exchange interaction between spins plays a role (left inset of Fig. 1). In an idealized experiment, as sketched in the right inset of Fig. 1, where two ferromagnets can come in direct contact without forming an interface anymore, we arrive in a conflicting situation: neighboring spins of a ferromagnetic material do not align parallel! Therefore, interesting physics may be involved in the problem. Thin ferromagnetic films separated by a structurally and chemically well defined spacer layer with a controlled thickness in the nanometer range allow to study ferromagnets in close proximity. As we will see below, this arrangement reveals a new type of magnetic interaction, which — as it is often the case on atomic length scales — is a quantum effect as it reflects the wave nature of electrons.

1.1. Phenomenological Description

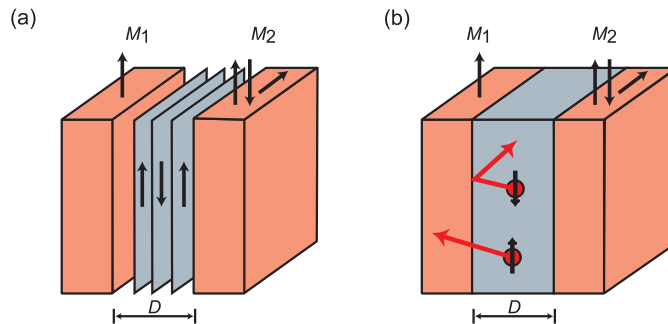


Fig. 2. Two types of interlayer coupling depending on the nature of the interlayer. (a) The interlayer is assumed to be antiferromagnetic with spin alignment as shown. (b) A paramagnetic or diamagnetic material for the interlayer is assumed. The magnetization \vec{M}_1 points upwards. Due to the coupling \vec{M}_2 can show the alignments parallel and antiparallel (or even perpendicular) with respect to \vec{M}_1

Ferromagnetic films can couple across nonmagnetic interlayers in various ways. When the lateral dimensions are sufficiently small, magnetostatic coupling aligning the magnetizations antiparallel can arise due to the fringing fields at the edge of the sample, similar to the macroscopic situation discussed above. Ferromagnetic interlayer coupling trying to align the magnetizations parallel, on the other hand, can occur as a result of local stray fields produced by interface roughness. This so-called orange peel — or Néel type — coupling is also of dipolar nature. It is probably present in many cases, but not our main interest here. Generally it is difficult to trace the origin of ferromagnetic interlayer coupling. There is always the extrinsic possibility that ferromagnetic bridges across the nonmagnetic spacer exist, which give rise to direct exchange between the ferromagnetic films. An intrinsic coupling mechanism can be obtained, if we extend the idea of direct coupling at interfaces to a layered structure consisting of a thin antiferromagnetic layer with ferromagnetic material on both sides. This situation is displayed in Fig. 2(a). Obviously, the coupling of the ferromagnets across the antiferromagnet will be an-

tiferromagnetic (ferromagnetic) for even (odd) number of monolayers of the antiferromagnet. This oscillation of the coupling between antiferromagnetic and ferromagnetic with a period of two monolayers has indeed been observed for interlayers of antiferromagnetic Cr [1] and Mn [2] when the growth is sufficiently good. This mechanism is referred to as proximity magnetism [3]. However, for somewhat reduced growth quality, longer coupling periods of the order of 10 Å are observed which cannot be explained on the basis just described. This new aspect is even more distinct in the cases of coupling across metallic paramagnetic or diamagnetic interlayers, where a description based on static magnetic order in the interlayer is not possible. As we will see below, in these cases coupling is due to spin-dependent electron reflectivity at the interfaces as sketched in Fig. 2(b). In 1990 the oscillatory nature of this new type of coupling P the interlayer exchange coupling (IEC) was recognized as a general phenomenon [1]. Experiments showed that IEC of ferromagnetic 3d metals across interlayers can be phenomenologically described by an areal energy density σ_{IEC} given by

$$\sigma_{\text{IEC}} = -J_1 \cos(\theta) - J_2 \cos^2(\theta). \quad (3)$$

Here, θ is the angle between the magnetizations of the films on both sides of the spacer layer. The parameters J_1 and J_2 describe the type and the strength of the coupling. If the J_1 term dominates, then from the minima of Eq. (3) the coupling is ferromagnetic (antiferromagnetic) for positive (negative) J_1 . If the J_2 term dominates and is negative, we obtain 90°-coupling. The first term of Eq. (3) is often called bilinear coupling and the second biquadratic coupling. Biquadratic coupling is thought to be mainly due to interface roughness and will not be further considered here (see Ref. [1]).

1.2. Microscopic Picture: Quantum Well States

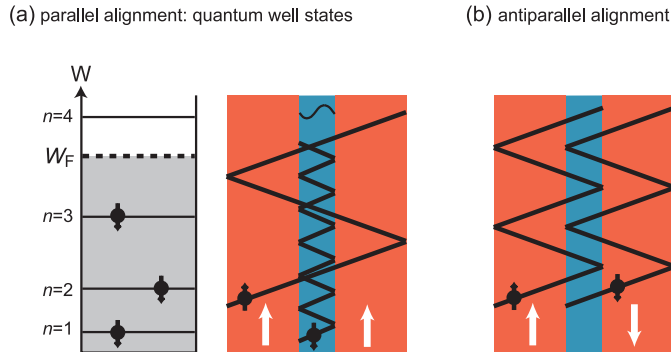


Fig. 3. Spin-dependent reflectivity at the nonmagnetic/magnetic interfaces for the explanation of oscillatory coupling (a) for parallel and (b) for antiparallel alignment. The discrete energy levels of the quantum well states are also shown in (a)

IEC is an indirect exchange interaction mediated by the conduction electrons of the spacer layer. We consider the itinerant nature of electrons in transition metal ferromagnets, which gives rise to a spin-split band structure and spin-dependent reflectivities at the paramagnet/ferromagnet interfaces. The spin-dependent reflectivity is illustrated in Fig. 3, where it is assumed that majority (minority) electrons, i.e. electrons with spin parallel (antiparallel) to the local magnetization, are weakly (strongly) reflected at the interfaces. The reason for this

behavior is seen in Fig. 4. For the spin-up (majority) electrons there is a good match of the

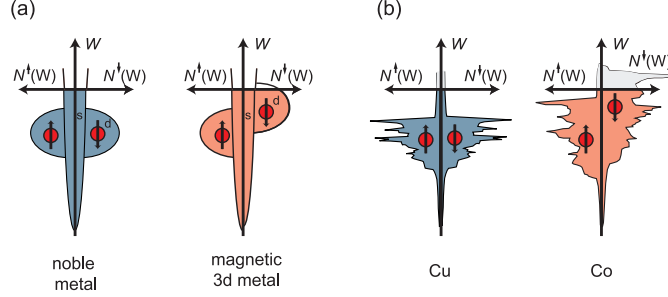


Fig. 4. (a) Schematic spin-split density of states (DOS) for a noble metal and a 3d transition metal representing the spacer and magnetic layer, respectively. The relative positions of the bands for spin-up and spin-down electrons give rise to spin-dependent reflectivity at the interfaces. (b) Realistic spin-split DOS for Cu and Co showing the qualitative features sketched in (a)

states in the ferromagnet and the interlayer (here represented by a noble metal) as indicated by the same position of the bands on the energy scale. A good match of the states means that states with similar symmetry, \vec{k} vector, and energy exist in both materials. Therefore, electrons in these states can more or less easily move from one material to the other. As it is always the case for an itinerant ferromagnet, the spin-down (minority) bands are shifted on the energy scale with respect to the spin-up (majority) bands due to the exchange interaction associated with the ferromagnetic order. Therefore, the good match with the bands in the interlayer is lost. In other words, minority electrons experience a higher potential step at the interface than majority electrons and are thus reflected with a higher probability. For the minority electrons this gives rise to quantum well states (QWS), i.e. there are spin-dependent interference effects like the formation of standing electron waves for certain interlayer thicknesses. But, QWS in the interlayer only form for parallel alignment of the magnetizations of the ferromagnetic layers [Fig. 3(a)] because only in this case the minority electrons are reflected on both sides of the spacer.

The description of QWS is similar to electrons in a one-dimensional potential well, except that for the time being we only consider states with a given momentum component perpendicular to the layers k_{\perp} . A justification for this restriction and a method to find the right k_{\perp} will be given below. The condition to form a standing wave in a well (i.e. a QWS) of thickness D is

$$k_{\perp}^{(n)} = n \frac{\pi}{D} \quad ; \quad n = 1, 2, \dots \quad (4)$$

These QWS correspond to discrete energy levels [left part of Fig. 3(a)]

$$W_n = \frac{\hbar^2}{2m} (k_{\perp}^{(n)})^2 = n^2 \frac{\hbar^2 \pi^2}{2mD^2} \quad ; \quad n = 1, 2, \dots \quad (5)$$

Upon increasing the spacer thickness D , these levels move downwards on the energy scale. Each time when a level crosses the Fermi energy W_F , the corresponding QWS are populated, and the energy of the electronic system increases. When the QWS level moves further below the Fermi energy, the energy again decreases until the next QWS level approaches the Fermi energy. For the parallel alignment the energy oscillates as a function of spacer thickness as shown by the green curve in Fig. 5. For the antiparallel alignment [Fig. 3(b)] the energy of the system does not show the oscillatory behavior (red curve in Fig. 5). In order to always take the configuration with the

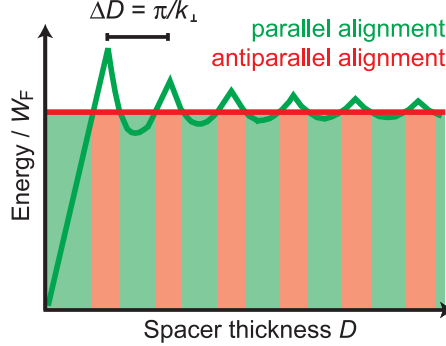


Fig. 5. Spacer thickness dependence of the energy of the electronic system (normalized to the Fermi energy W_F) as a function of the spacer thickness D for the parallel and antiparallel alignment. Green (red) areas indicate ferromagnetic (antiferromagnetic) coupling for the corresponding spacer thickness ranges. After Ref. [4]

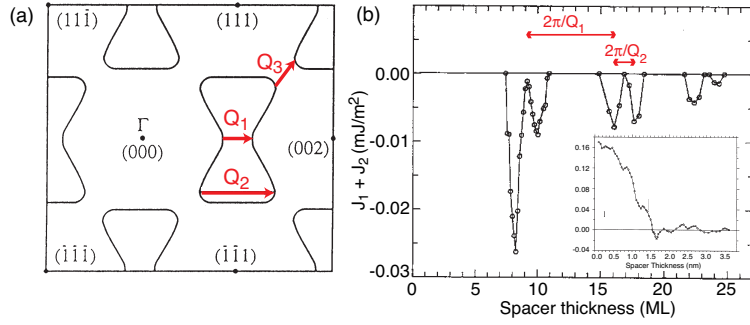


Fig. 6. (a) Cross section of the Fermi surface of Au with the critical spanning vectors Q_1 and Q_2 in [001] direction. (b) Coupling strength of Fe/Au-wedge/Fe(100) trilayers as a function of the Au interlayer thickness [5]. The inset includes ranges where the coupling is ferromagnetic ($J_1 + J_2 > 0$)

lowest energy the alignment switches between parallel and antiparallel, and hence the coupling oscillates. The oscillation period ΔD follows from Eq. (4) for $\Delta n = 1$: $\Delta D = \pi/k_{\perp}$. A more detailed theoretical treatment of IEC is given in Ref. [6]. The basic result is that the oscillation period(s) of the interlayer coupling can be predicted for realistic electronic band structures by considering the Fermi surface of the spacer material. One then finds that oscillatory coupling is related to a so-called critical spanning vector \vec{Q} in reciprocal space with the following properties: (i) \vec{Q} points perpendicular to the interface, (ii) \vec{Q} connects two sheets of the Fermi surface which are coplanar to each other, and (iii) \vec{Q} is in the first Brillouin zone. The last condition follows from Bloch's theorem and reflects the atomic periodicity of the spacer material. The oscillation period is given by $2\pi/Q$. For real materials, several \vec{Q}_i ($i = 1, 2, \dots$) may exist, each of them corresponding to a different oscillation period $2\pi/Q_i$. In this case, the experimentally measured coupling versus thickness curve is the superposition of all these oscillations. As an example we consider an Au spacer layer grown in [001] direction. For the Fermi surface of Au as shown in Fig. 6(a), there are two critical spanning vectors (\vec{Q}_1 and \vec{Q}_2) in the [001] direction. The

periods of the oscillatory coupling are given by $\Delta D_i = 2\pi/Q_i$. Figure 6(b) shows the result of an evaluation of remagnetization curves for a Fe/Au-wedge/Fe structure. The coupling is strongly ferromagnetic ($J_1 + J_2 > 0$) for small spacer thickness D_{Au} [inset of Fig. 6(b)], probably due to pinholes and magnetic bridges. For increasing D_{Au} the ferromagnetic coupling quickly decreases until there are oscillations around zero. Two oscillations with amplitudes that are attenuated as a function of the interlayer thickness are superimposed. The two oscillations periods, 2.5 and 8.6 ML, are in excellent agreement with the predictions based on Fig. 6(a). Apart from the interface quality the strength of the coupling depends also on many details of the participating Fermi surfaces. For a compilation of observed values of J_1 and the associated coupling period(s) see Table 1.

Table 1. Selection of observed bilinear coupling strengths and periods collected from the literature [1].

Sample	Maximum strength $-J_1$ in mJ/m ² (at spacer thickness in nm)	Periods in ML and (nm)
Co/Cu/Co(100)	0.4 (1.2)	2.6 (0.47); 8 (1.45)
Co/Cu/Co(110)	0.7 (0.85)	9.8 (1.25)
Co/Cu/Co(111)	1.1 (0.85)	5.5 (1.15)
Fe/Au/Fe(100)	0.85 (0.82)	2.5 (0.51); 8.6 (1.75)
Fe/Cr/Fe(100)	>1.5 (1.3)	2.1 (0.3); 12 (1.73)
Fe/Mn/Fe(100)	0.14 (1.32)	2 (0.33)
Co/Ru(0001)	6 (0.6)	5.1 (1.1)
Co/Rh/Co(111)	34 (0.48)	2.7 (0.6)

2. Giant Magnetoresistance (GMR)

The giant magnetoresistance (GMR) effect describes the finding that in layered magnetic structures the resistivity depends on the relative alignment of the magnetizations of adjacent ferromagnetic layers [7]. The pioneering experiments are displayed in Fig. 7.

2.1. Phenomenological Description

At zero field adjacent Fe layers align antiparallel due to antiferromagnetic interlayer exchange coupling (Sect. 1.) across the Cr spacer, whereas a large enough external magnetic field saturates the sample and forces the Fe layers into a parallel configuration. The transition from the antiparallel to the parallel alignment is accompanied by a drastic change of the resistivity. The blue curve in Fig. 7(b) shows the so-called anisotropic magnetoresistance (AMR) effect of a 250 Å Fe layer for comparison. AMR describes the dependence of the electric resistivity on the angle between the current and the magnetization direction. AMR is a volume effect discovered in 1857 and applied in read-heads since the 1970's. The much larger response of the layered structures is the reason why the new effect was dubbed giant magnetoresistance. The measurements in Fig. 7 represent the simultaneous, but independent discovery of GMR, for which Albert Fert (University of Paris-Sud) and Peter Grünberg (Research Center Jülich) were awarded the Nobel Prize in Physics in 2007.

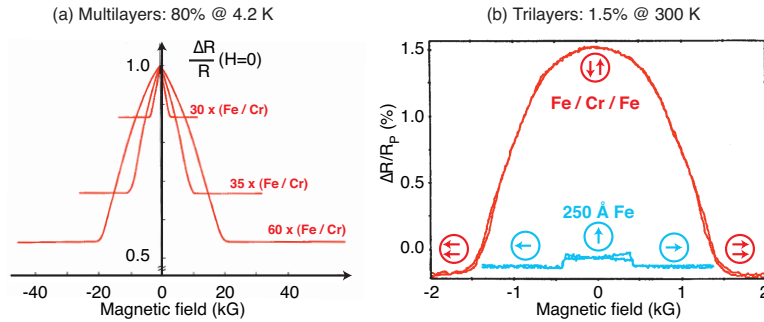


Fig. 7. First observations of the GMR effect in (a) Fe/Cr multilayers [8] and (b) Fe/Cr/Fe trilayers [9]

Apart from antiferromagnetic IEC the antiparallel alignment at small fields can also be achieved by hysteresis effects. In the latter case one film is magnetically pinned (e.g. by the exchange bias effect due to an antiferromagnet), whereas the magnetization of the other is free to rotate when an external field is applied. Such arrangements [inset of Fig. 8(a)] are called spin valves and are relevant for applications. The magnetization loop and the corresponding GMR signal of the spin valve structure are displayed in Fig. 8. The steep slope of resistance near zero field provides a sensitive signal to measure small magnetic fields. If we denote by R_P the resistance for parallel alignment of adjacent ferromagnetic films and by R_{AP} the same for antiparallel alignment, then the strength of GMR effects is usually quoted in terms of

$$\frac{\Delta R}{R_P} = \frac{R_{AP} - R_P}{R_P}. \quad (6)$$

Mostly, the resistance is highest for antiparallel alignment yielding a positive $\Delta R/R_P$ corresponding to the so-called normal GMR effect. But there are also cases where the situation is reversed and $\Delta R/R_P$ becomes negative. This is called the inverse GMR effect. The GMR effect has been investigated in two different geometries, namely the CIP (Current In Plane) and the CPP (Current Perpendicular Plane) geometry. The relative effect is stronger in the CPP geometry. However, due to the extremely unfavourable geometric conditions (lateral dimensions some orders of magnitude larger than the film thickness), the voltage drop perpendicular to the layers — CPP geometry — is very difficult to detect without special structuring. Representative and record values for the GMR effect as defined by Eq. (6) both in the CIP and the CPP geometry have been compiled from the literature in Table 2.

2.2. Microscopic Picture: Spin-dependent Scattering

The mechanism leading to GMR can be understood within Mott's two current model [7, 12], which assumes two independent current channels for spin-up and spin-down electrons. Due to their Fermi velocity the conduction electrons propagate with high speed but arbitrary direction through the layered structure. A current results from a much smaller drift velocity in the direction of the applied electric field. In Fig. 9 paths between two reflections at outer surfaces are shown with scattering events in between. In order not to confuse the picture the changes in direction due to the scattering events are suppressed. Because of the dominance of the Fermi velocity, the schematic representation and the substitutional circuit diagrams in Fig. 9 hold for both CIP

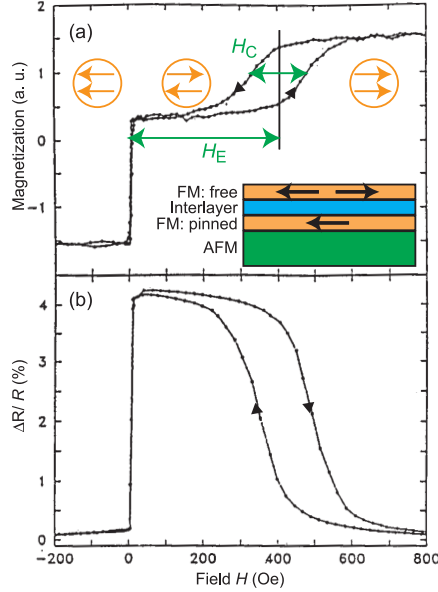


Fig. 8. (a) Hysteresis loop $M(H)$, and (b) magnetoresistance $\Delta R/R$ of a $\text{Fe}_{20}\text{Ni}_{80}$ (6 nm) / Cu (2.2 nm) / $\text{Fe}_{20}\text{Ni}_{80}$ (4 nm) / FeMn (7 nm) GMR spin valve at room temperature. The FeMn layer is antiferromagnetic. The spin valve structure is schematically shown in the inset of (a). Orange pairs of arrows indicate the relative alignment of the magnetizations of the magnetic films. After Ref. [10]

and CPP geometry. The scattering processes are the cause of electric resistance. Only states near the Fermi energy contribute to the electric conductivity because they can reach empty final states just above the Fermi energy after a scattering event. In order to demonstrate how spin-dependent scattering leads to the GMR effect, we use in the following a simple – albeit unrealistic – consideration whose main argument is nevertheless valid in reality. In Fig. 9(a) it is assumed that only minority electrons (spin antiparallel to the local magnetization) are scattered at the magnetic/nonmagnetic interfaces. The origin for the spin-dependent behaviour can again be found in the spin-split DOS of 3d transition metals (Fig. 4). They show different numbers of final states (density of states near the Fermi energy) for majority and minority electrons and, hence, different spin-dependent scattering probabilities. Thus, in our simplified picture, for parallel alignment of the magnetizations, majority electrons are not scattered at all, leading to a short circuit ($R = 0$) of the associated current. Therefore, the resistivity for the total current vanishes, too, as can be seen in the lower part of Fig. 9(a), where the two spin channels are represented by two resistors in parallel connection. For antiparallel alignment of the magnetizations [Fig. 9(b)] there are scattering events for both types of electrons. Hence, the resistivity for the total current is finite. It is clear that even if the above strict condition is relaxed, the resistivity will be higher for antiparallel alignment as compared to the parallel one. For the whole discussion we have assumed that the spin direction of the electrons is conserved inside the spacer layer. Since there is scattering in the spacer layer as in any normal metal, this assumption only holds when the spacer layer is thinner than the characteristic length scale for spin conservation, the spin diffusion length. This condition implicates that GMR can only exist

Table 2. Representative values for GMR ratios. Geometry is CIP unless specially marked with CPP (see text). Auxiliary layers which are not directly active in the GMR effect are mostly omitted. Numbers in brackets indicate the layer thickness in Å. Compiled from Ref. [11].

Sample	$\Delta R/R_P$ (%)	Temperature (K)
[Fe(4.5)/Cr(12)] ₅₀	220	1.5
	42	300
[Co(10)/Cu(10)] ₁₀₀	80	300
Co(30)/Cu(19)/Co(25)	19	300
Co ₉₀ Fe ₁₀ (40)/Cu(25)/Co ₉₀ Fe ₁₀ (8)...	7	300
NiFe(100)/Cu(25)/Co(22)	4.6	300
... CoFe/AgCu(15)/CoFe...	4–7	300
[Co(15)/Cu(12)] _n CPP	170	4.2
[Co(12)/Cu(11)] ₁₈₀ CPP	55	300

for spacer thicknesses of the order of a few nanometers at most. An animation explaining this simple picture of GMR and how GMR is used in read-heads of high-density harddisks is available on the internet [13].

3. Tunnel Magnetoresistance (TMR)

The first TMR effect of 14% was observed already in 1975 by Jullière [14] in Fe/Ge/Co junctions. But the effect was only observable at liquid He temperature. Triggered by the success of GMR, ferromagnet/insulator/ferromagnet structures were revisited in 1995 and up to 18% TMR effect could be observed for the first time at room temperature [15, 16].

3.1. Phenomenological Description

The basic configuration for tunnel magnetoresistance consists of two ferromagnetic electrodes — here in the form of thin films — separated by an insulating or semiconducting barrier as shown in the upper part of Fig. 10. If a voltage V (several tens to hundreds mV) is applied across the stack a small quantum-mechanical tunneling current can flow across the barrier. This means that — unlike GMR — the TMR effect is always observed in CPP geometry. The magnitude of the tunneling current is related to the overlap of the exponentially decaying wave functions inside the barrier. Therefore, the current exponentially decreases with the barrier thickness. Typical barrier thicknesses are of the order of 1 nm. The tunneling resistance is found to depend on the relative orientation of the magnetizations on both sides of the barrier [17]. Like in the case of GMR we denote by R_P the resistance for parallel magnetizations, and by R_{AP} the resistance for antiparallel alignment. The size of the TMR effect is determined in the same way as for GMR [compare Eq. (6)]

$$\frac{\Delta R}{R_P} = \frac{R_{AP} - R_P}{R_P}. \quad (7)$$

Fig. 11 displays typical TMR curves for systems with transition metal electrodes and AlO_x barriers. After annealing the structure at 300 °C, the TMR ratio is around 50% at room temperature. The record value for AlO_x barriers of 70% at room temperature is achieved by using

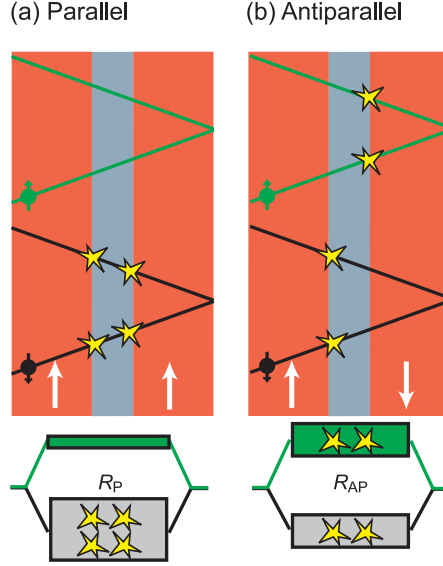


Fig. 9. Simplistic picture of spin-dependent scattering for the explanation of the GMR effect. Only minority electrons are scattered as schematically indicated by the yellow stars. Majority electrons are not scattered and cause a short circuit effect, which appears for parallel alignment of the magnetizations (a) but not for antiparallel alignment (b). The substitutional circuit diagrams in the lower part for the total resistivities, R_P and R_{AP} , yield the relation $R_P < R_{AP}$ and hence a normal GMR effect. This picture holds for both CIP and CPP geometry

amorphous CoFeB electrodes [19]. However, much higher TMR values have been found in epitaxial Fe/MgO/Fe(001) structures and will be discussed in Sect. 3.3.

3.2. Microscopic Picture: Spin-dependent Tunneling

The TMR effect can be understood on the basis of spinpolarized tunneling. When the spin is conserved during tunneling, a spin-up (spin-down) electron can only tunnel from an initial spin-up (spin-down) state to an unoccupied spin-up (spin-down) final state. As we will see, TMR arises from the imbalance between the number of spin-up and spin-down electrons that contribute to the tunneling current. Therefore, we define the spin polarizations P_L and P_R of the left and right electrodes

$$P_{L,R} = \frac{N_{L,R}^\uparrow - N_{L,R}^\downarrow}{N_{L,R}^\uparrow + N_{L,R}^\downarrow}. \quad (8)$$

Here, $N_{L,R}^\uparrow$ and $N_{L,R}^\downarrow$ denote the number of states in an energy window at the Fermi level with a width given by the applied voltage V . Only states within this window can contribute to the tunneling current. In Fig. 10 the dark green and red colored areas in the vicinity of the Fermi level correspond to these quantities. It is assumed that a positive voltage V is applied to the right electrode. The green and red arrows represent the spin-up and spin-down tunneling currents, respectively, with their thickness indicating the magnitude of the currents. For instance, the spin-up current in the parallel configuration is proportional to the product $N_L^\uparrow N_R^\uparrow$ (green arrow in the left hand part). Obviously, the parallel alignment on the left hand side of Fig. 10 gives

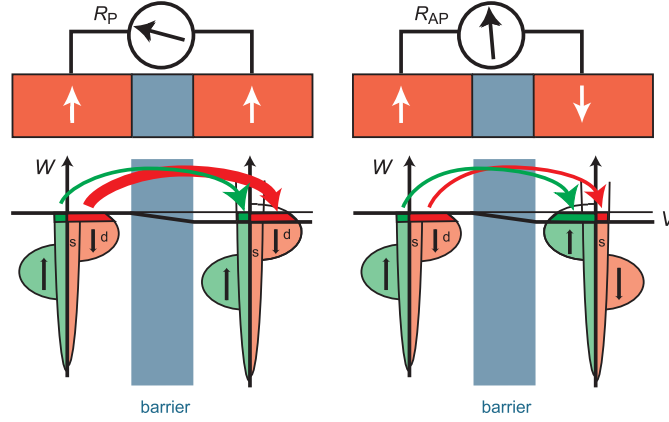


Fig. 10. Assuming energy and spin conservation during the tunneling process, the tunneling current can be decomposed into spin-up (green arrows) and spin-down (red arrows) contributions. Their magnitudes (represented by the thickness of the arrows) are determined by the number of available initial and final states for each spin channel, here given by the simplified DOS of 3d metals. Hence, the total current and the resistance of the tunnel junction depend on the alignment of the magnetizations

rise to a larger total current and, thus, to the smaller tunneling resistance. R_P and R_{AP} are inversely proportional to the total current (i.e. the sum of the spin-up and spin-down currents) and can be written as

$$R_P \propto \frac{V}{N_L^\uparrow N_R^\uparrow + N_L^\downarrow N_R^\downarrow} \quad ; \quad R_{AP} \propto \frac{V}{N_L^\uparrow N_R^\downarrow + N_L^\downarrow N_R^\uparrow}. \quad (9)$$

After inserting these expressions in Eq. (7) and some rearranging, $\Delta R/R_P$ can be expressed by the polarizations defined in Eq. (8)

$$\frac{\Delta R}{R_P} = \frac{R_{AP} - R_P}{R_P} = \frac{2P_L P_R}{1 - P_L P_R}. \quad (10)$$

This expression for the TMR ratio is nowadays called Jullière's relation after the inventor of this model [14]. Usually ΔR is positive, and therefore the TMR effect is called normal. For the inverse effect [20, 21], which has also been observed, ΔR is negative. In Figs.10 and 11 the effect turns out to be normal, but an inverse effect can result if the magnetic electrodes on both sides of the barrier were different in such a way that the P_L and P_R have opposite signs [see Eq. (10)]. Examples are given below. The TMR effect usually decreases as a function of bias voltage and temperature, the origin of both effects is so far not clear. Spinscattering in the interlayers, density-of-states effects as well as the excitation of spinwaves have been considered.

3.3. Beyond Jullière's Model

Obviously, Jullière's model is very simple, and it is not surprising that several experimental observations cannot be consistently explained in the framework of this model. For instance, it is not clear how to obtain the relevant values for P_L and P_R . Polarizations determined from TMR measurements using the Jullière relation [Eq. (10)] are sometimes in strong disagreement (in some cases even concerning the sign of P) with polarizations determined by other techniques. This

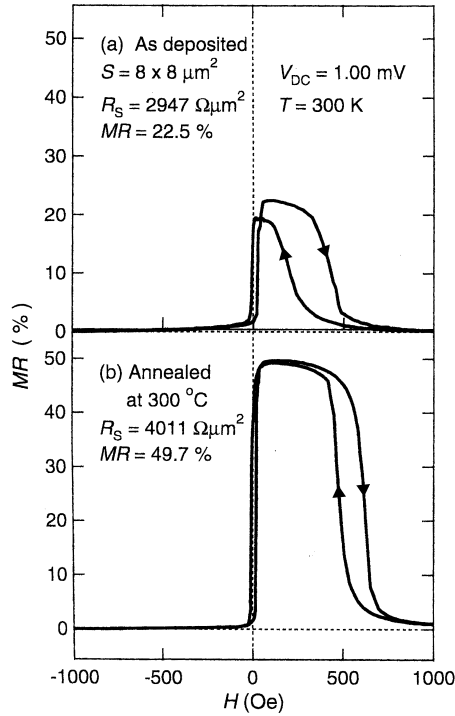


Fig. 11. TMR curves measured at room temperature for films of $\text{Co}_{75}\text{Fe}_{25}$ (4 nm) across barriers of Al_2O_3 (0.8 nm). S = sample area, R_S = sheet resistance for parallel magnetization alignment, V_{DC} = bias voltage, $MR = \Delta R/R_P$. The observed increase of TMR from the as deposited state (a) to the annealed state (b) is an often observed effect and is likely to be related to improvements of the interface configuration. The asymmetry with respect to $H = 0$ arises from exchange bias due to a 10 nm-thick, antiferromagnetic IrMn layer. From Ref. [18]

reflects the fact, that the polarization of a material is not a universal quantity. It can strongly depend on the experiment under consideration, because different energy ranges, different orbital momentum selection rules, and different parts of the sample determine the polarization measured by different techniques. For TMR, only the polarizations of the electronic states right at the interfaces including possible interface states are important. The energy range to be considered is given by the applied voltage V , and the tunneling probability is enhanced for states with maximum momentum perpendicular to the barrier. Furthermore, the Jullière model does not consider realistic barriers. Note that the barrier properties do not explicitly appear in Eq. (10). However, the complex Fermi surface of the barrier material may modify the (spin-dependent) decay length of the wave functions compared to a vacuum barrier. This influence can change the relative contribution of different states to the tunneling current, and thus the degree or even the sign of the polarization of the tunneling current. An impressive demonstration of the influence of the interlayer has been given by De Teresa et al. [21] and is shown in Fig. 12. In these experiments the two ferromagnetic electrodes are always made of Co and $\text{La}_{0.7}\text{Sr}_{0.3}\text{MnO}_3$, but different barrier materials are used. For SrTiO_3 and $\text{Ce}_{0.69}\text{La}_{0.31}\text{O}_{1.845}$ barriers the TMR was found to be inverse [Fig. 12(a) and (b)], whereas it was normal for Al_2O_3 and $\text{Al}_2\text{O}_3/\text{SrTiO}_3$ barriers [Fig. 12(c) and (d)]. These experiments clearly prove that TMR also depends on the barrier material in clear

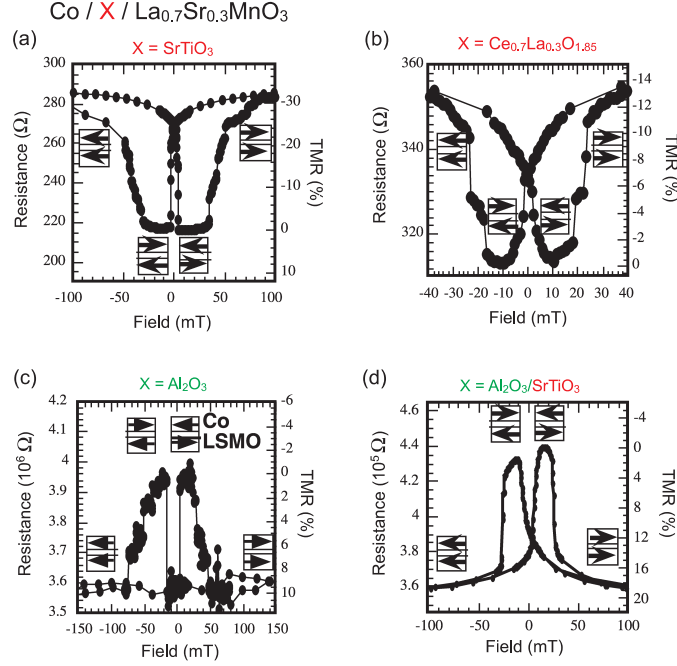


Fig. 12. TMR of $\text{Co}/\text{X}/\text{La}_{0.7}\text{Sr}_{0.3}\text{MnO}_3$ structures with (a) $\text{X} = \text{SrTiO}_3$, (b) $\text{X} = \text{Ce}_{0.69}\text{La}_{0.31}\text{O}_{1.845}$, (c) $\text{X} = \text{Al}_2\text{O}_3$, and (d) $\text{X} = \text{Al}_2\text{O}_3/\text{SrTiO}_3$. The material-dependent change from the inverse (a,b) to the normal (c,d) TMR effect indicates the influence of the Co/insulator interface. After Ref. [21]

contrast to Jullière's model. The spin polarizations P_L and P_R must thus be related to interface states, which play a major role for the chemical bonding at the interfaces.

The limited validity of Jullière's model also became obvious when extremely high TMR ratios of up to 220% at room temperature for epitaxial [23] or highly oriented [24] $\text{MgO}(001)$ barriers and Fe or CoFe electrodes were reported. The high TMR ratios translate with the Jullière relation [Eq. (10)] into spin polarizations $P_{L,R} \approx 70\%$, which are definitely too high to be identified with bulk spin polarizations of Fe or CoFe alloys of typically about 40%. The experiments, however, confirm a theoretical prediction [22] that single-crystalline, epitaxial MgO barriers in combination with $\text{Fe}(001)$ electrodes would yield huge TMR ratios of hundreds or even thousands of percent. In epitaxial junctions the tunneling is coherent, meaning that the symmetry of the states is conserved across the tunneling barrier. Therefore, specific features in the band structures of MgO and Fe can be exploited: (i) The complex band structure of MgO yields a much smaller exponential decay inside the barrier for the electronic states with Δ_1 symmetry compared to all other symmetries [Fig. 13(a)]. Therefore, the tunneling current in $\text{Fe}/\text{MgO}/\text{Fe}(001)$ is predominantly carried by Δ_1 states. (ii) In Fe, the Δ_1^\uparrow and Δ_1^\downarrow bands show strong exchange splitting, and only the majority Δ_1^\uparrow band crosses the Fermi level [Fig. 13(b)]. This leads to a strong spin selection in the tunneling process, and hence a TMR ratio as high as 500% at 300 K (1010% at 5 K) [25]. Although the combination of MgO with Fe and Co (and related Fe-based alloys with bcc structure, e.g. CoFe or CoFeB) seems to be a particular case — the MgO barrier selects via "symmetry filtering" specific bands of the ferromagnetic electrodes, which happen to be highly spin-polarized at the Fermi level — this material system is intensely

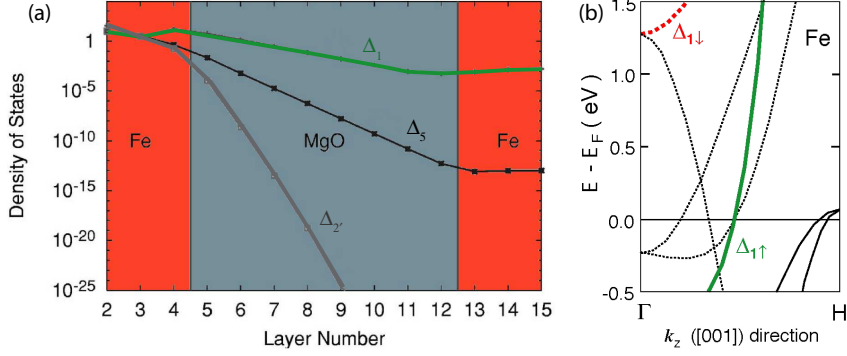


Fig. 13. (a) States with Δ_1 -symmetry decay slowest inside the MgO barrier. The density of states of all other symmetries is suppressed by orders of magnitude [22]. (b) In Fe the bands with Δ_1 -symmetry are exchange-split and only the majority Δ_1^\uparrow band crosses the Fermi energy

discussed for applications such as the magnetic random access memory (MRAM).

4. Spin-Transfer Torque (STT)

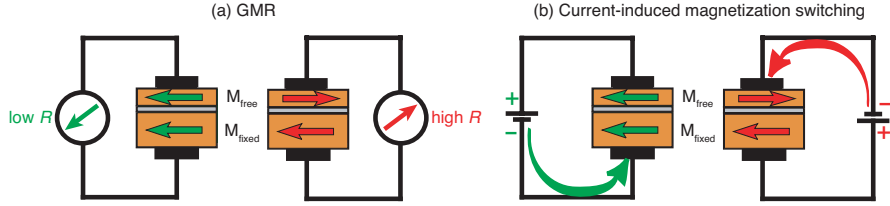


Fig. 14. Phenomenology of (a) GMR and (b) current-induced magnetization switching as a manifestation of STT effects. (a) The electric resistance of a trilayer structure consisting of two ferromagnets separated by a nonmagnetic, metallic interlayer depends on the alignment of the layer magnetizations. (b) The stable alignment of the magnetizations depends on the polarity, i.e. the direction, of the current flowing perpendicularly through the trilayer

Magnetoresistance effects like GMR and TMR describe the influence of the relative magnetization alignment between adjacent magnetic layers on the current flow, i.e. the resistance. The spin-transfer torque (STT) effects to be discussed in this section represent a reciprocal interaction (Fig. 14): In a device with inhomogeneous magnetization profile a strong current can transfer spin momentum between different parts of the device and thus exerts a torque on the local magnetization and thereby influences the magnetization configuration. Current-induced magnetization switching, excitation of steady magnetization oscillations, and current-induced domain wall motion are experimentally observable manifestations of the current-driven magnetization dynamics due to STT [26]. Consequently, the spin-transfer torque provides a means to control magnetization states, whereas GMR and TMR can sense them. To this end, the spin-transfer torque extends the toolbox for spintronics and magnetoelectronics by a further complementary functionality. For instance, this technique is currently the subject of intense discussion as an efficient, fast, scalable and reliable means for writing the individual cells in magnetic random

access memories (MRAM), which may also simplify the device architecture.

4.1. Phenomenological Description of STT

In 1996 Slonczewski [27] and Berger [28] predicted that a spin-polarized current propagating into a ferromagnetic layer exerts a torque on the layers's magnetization, due to the exchange interaction between the electrons and the local magnetic moments. In layered metallic systems with alternating magnetic and non-magnetic layers, a current flowing perpendicular to the plane of the layers (CPP-geometry) is polarized by one ferromagnetic layer and transfers spin angular momentum to another ferromagnetic layer, where the transferred momentum acts as a torque on the magnetization. This effect is called spin-transfer torque. For this torque to be sufficient to perturb the magnetization from equilibrium, large current densities ($> 10^7$ A/cm²) are required. If two stable equilibria for the magnetization exist (e.g. due to a uniaxial anisotropy), the STT can reversibly switch the magnetization between the two equilibrium positions. This magnetic switching scheme does not require an external magnetic field. Its phenomenology is shown in Fig. 14(b). We consider two ferromagnetic layers separated by a non-ferromagnetic spacer with a thickness less than its spin diffusion length. The ferromagnetic layers are different in such a way (e.g. thickness or coercive field), that one of them can be remagnetized more easily than the other. We distinguish the two layers in the following by calling them free and fixed and draw them as a thinner and thicker layer, respectively. When electrons flow from the fixed to the free layer, the magnetization of the free layers aligns parallel to the magnetization of the fixed layer and this alignment is stabilized. When the current direction is reversed, however, the antiparallel alignment is more stable and adopted as will be explained in Sect. 4.2. Thus, a magnetization reversal can be induced by reversing the polarity of the DC current flowing through the layers.

An experimental arrangement for the observation of current-induced switching is displayed in Fig. 15(a). The sample consists of a column of layers from various materials stacked on top of each

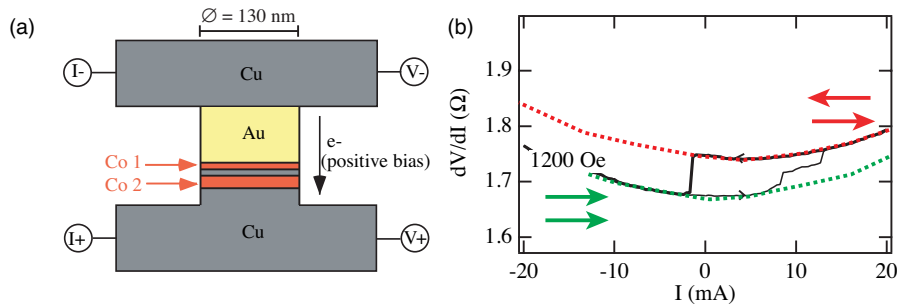


Fig. 15. (a) Schematic pillar device with two thin Co layers (Co 1 and Co 2) separated by a 6 nm thick Cu layer. (b) The dV/dI measurements as a function of the current through the column device yields the relative alignment of the magnetic layers via the GMR effect. At positive bias electrons flow from the thin Co 1 to the thick Co 2 layer. For large enough currents the Co 1 layer switches to antiparallel alignment as indicated by the higher resistance. For negative bias parallel alignment and a lower resistance is observed. After Ref. [29]

other as shown. A current can be fed in by leads I^- and I^+ , and the voltage drop is measured at V^- and V^+ . There is a thin Co layer, Co 1, with a thickness of 2.5 nm and a thick Co layer, Co 2, of 10 nm thickness. The Cu spacer in between is 6 nm thick. The lateral diameter of the column

is about 100 nm. This lateral restriction is required to obtain the necessary high current density (of the order of 10^8 A/cm²) to establish a steady (constant current) nonequilibrium situation. As shown in Fig. 15(b), the relative orientation of the Co layers can be measured via the GMR effect of the Co1/Cu/Co2 trilayer. At negative bias electrons flow from the thick to the thin Co layer and stabilize the parallel magnetization alignment, which yields a low dV/dI . At positive bias the parallel alignment is destabilized, Co1 switches to the antiparallel alignment at a sufficiently large current, and dV/dI increases. Upon reducing the current [thick line in Fig. 15(b)], hysteretic behavior is observed such that Co1 switches back only at a negative current.

4.2. Physical Picture of STT: Absorption of the Transverse Spin Current Component

Being aware of the high current densities, one might suppose that the Oersted field generated by the current is responsible for the switching behavior. The circumferential Oersted field favors for a magnetic disk the so-called magnetic vortex state, which is characterized by an in-plane circulation of the magnetization and a small perpendicularly magnetized core region. This arrangement minimizes the stray field energy because no magnetic flux penetrates the surface of the disk except in the small core region. However, switching into vortex states due to the Oersted field has the wrong symmetry: Both current polarities would lead to a vortex-like magnetization state but with opposite sense of rotation. Nevertheless, they would result in the same GMR response, and a symmetric behavior for positive and negative currents is expected in clear contrast to the data in Fig. 15(b). Furthermore, the strongest Oersted field occurs at the pillar circumference and scales like I/d , where I is the current and d the pillar diameter. The STT effect scales like the current density I/d^2 and therefore becomes stronger below a certain structure size d_c . Theoretical estimates and available experiments suggest a d_c of the order of 100 nm. This fundamental size restriction coincides with the possibilities of e-beam lithography and at the same time yields the needed current densities at technically convenient current amplitudes [10 mA in an area of $(100\text{ nm})^2$ correspond to about 10^8 A/cm²]. In practice one always has to be aware of the presence of the Oersted field and has to take its possible influence into account.

In order to develop a physical picture for the spin-torque transfer effects, we start by considering a spinpolarized current that enters a ferromagnet from a metallic non-magnet. The situation is sketched in Fig. 16(a). The incident current is polarized along an axis tilted by the angle θ with respect to the magnetization \vec{M} of the ferromagnet. The (normalized) wave function of an polarized electron can be written as a superposition of spin-up and spin-down spinor components with respect to the quantization axis defined by \vec{M} . The amplitudes are $\cos(\theta/2)$ and $\sin(\theta/2)$, respectively, and correspond to a transverse component of the spin vector given by $\sin(\theta)$. At the interface to the ferromagnet the potential experienced by the electron changes and becomes spin-dependent. Therefore, the transmitted and reflected wave functions are different superpositions of spin-up and spin-down spinor components compared to the incident wave function. This leads unavoidably to different transverse spin components and thus to a discontinuity in the transverse spin current. The “missing” transverse spin current is absorbed at the interface and acts as a torque on the magnetization. This effect occurs for each electron individually and is called spin filtering [27]. Figure 16(a) shows the spinors in the extreme case of perfect spin filtering. In realistic cases, roughly 50 % of the transversal component is absorbed, and the transmitted as well as reflected currents still carry transversal components [30]. The actual current polarization of the transmitted and reflected currents is obtained by summing over all conduction electrons.

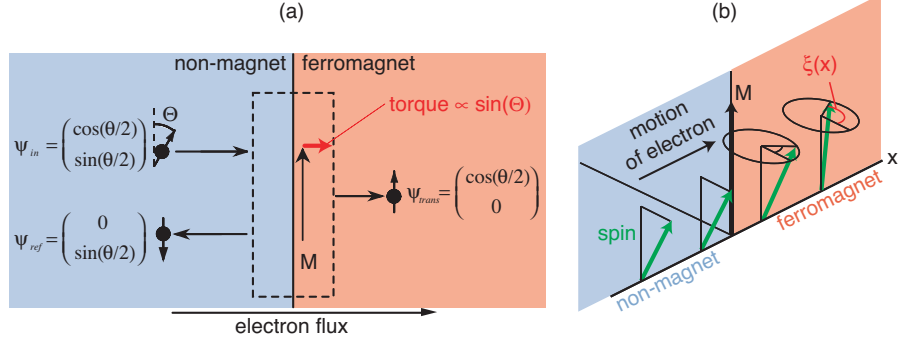


Fig. 16. Two effects contributing to the absorption of the transversal spin current component at the interface between a non-magnet and a ferromagnet. (a) Spin filtering: The incoming Ψ_{in} , transmitted Ψ_{trans} , and reflected Ψ_{ref} spinors for the idealized case of perfect spin filtering are indicated. The absorbed transversal spin current is proportional to $\sin(\theta)$ and acts as a torque on the interface magnetization. (b) Spatial precession of the spin in the ferromagnet: The phase ξ is constant in the non-magnet, but increases in the ferromagnet with distance x from the interface

This introduces two additional effects. The first arises because the reflection and transmission amplitudes at the interface are complex and depend on the \vec{k} vector of the considered electronic state. This means that the spin of an incoming electron rotates upon reflection and transmission by a \vec{k} -dependent angle. The cancellation, which occurs when we sum over all \vec{k} -states, reduces the net outgoing transverse spin current. This is an entirely quantum mechanical phenomenon, for which there is no classical analog. A second effect arises because spin-up and spin-down electrons on the Fermi surface have the same wave vector $k_{\uparrow} = k_{\downarrow}$ in the non-magnet but no longer when they enter the ferromagnet, $\Delta k = k_{\downarrow} - k_{\uparrow} \neq 0$. This is a consequence of the spin-split DOS. The two components are coherent, and a spatial phase $\xi(x) = \xi_0 + \Delta k x$ builds up [Fig. 16(b)] corresponding to a precession of the spin vector in space. The precession frequency is \vec{k} -dependent, i.e. varies with the position of the considered state on the Fermi surface. Therefore, when we sum over all conduction electrons, the transverse spin component is almost completely cancelled out after propagation by a few lattice constants into the ferromagnet.

Taking all three effects – (i) spin filtering, (ii) rotation of the reflected and transmitted spin, and (iii) spatial precession of the spin in the ferromagnet – together, to a good approximation, the transverse component of the transmitted and reflected spin currents are zero for most systems of interest. Thus, the incoming transverse spin current is absorbed by the interface and acts as a current-induced torque on the magnetization. A comprehensive theoretical treatment of these effects is given in [30].

Up to now we have assumed that the incident current is polarized. In the experiment this can be achieved by a second ferromagnetic layer with a slightly tilted magnetization (angle θ). The spin polarization is not modified in the non-magnetic spacer layer provided the spacer layer thickness is below its spin diffusion length to prevent significant depolarization by spin-flip scattering. In Fig. 17 we consider a trilayer structure very similar to the experimental setup of Fig. 15. In Fig. 17(a) the electrons flow from the fixed to the free layer. A current polarized by the fixed layer (1) hits the free layer and transfers its transversal component as a torque to the free layer. Part of the current is transmitted (2) and another part is reflected (3). This reflected current can now be considered as a polarized current impinging on the fixed layer. Again, the

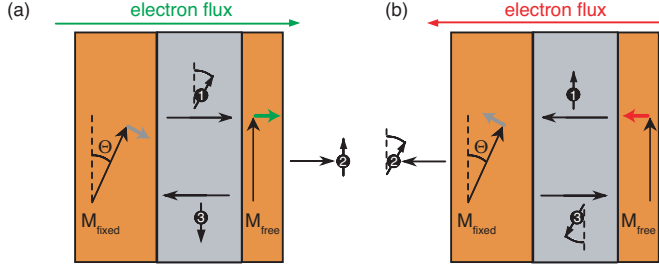


Fig. 17. Physical picture of the current-induced magnetization switching. Orange regions represent the two ferromagnetic layers. Due to the assumed asymmetry \vec{M}_{fixed} does not respond to the torque (short gray arrows) acting on it, whereas \vec{M}_{free} can follow the torque (short green and red arrows). The numbers in the spins refer to the sequence of the description. (a) and (b) show the situation for opposite electron flux directions, which result in stable parallel or stable antiparallel alignment, respectively

transversal component will be absorbed and acts as a torque on the fixed layer. However, due to the assumed asymmetry the fixed layer will resist to the torque, and only \vec{M}_{free} rotates until it reaches the stable parallel alignment with respect to \vec{M}_{fixed} . For the opposite direction of the electron flux in Fig. 17(b) we obtain a similar situation but the torques point in opposite directions. Therefore, the stable state corresponds to the antiparallel alignment of \vec{M}_{free} and \vec{M}_{fixed} . Note, that in this case the torque on \vec{M}_{free} arises from the current, which first has been reflected from the fixed layer. Obviously, the asymmetry (fixed \longleftrightarrow free) plays an important role, which is very reasonable because “left” and “right” cannot be distinguished for the symmetric case.

4.3. Extended Gilbert Equation

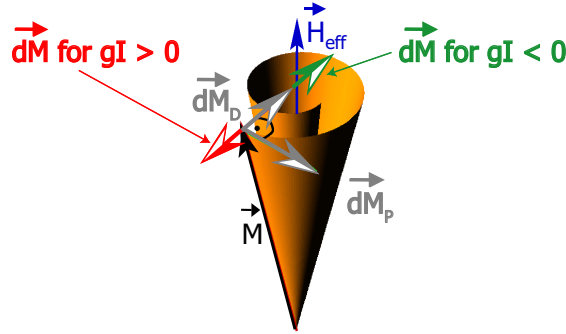


Fig. 18. Motion of a magnetization vector \vec{M} in an effective field \vec{H}_{eff} . The first term in Eq. (11) gives rise to the tangential torque $d\vec{M}_P/dt$ driving the precession. The second term $d\vec{M}_D/dt$ points in radial direction and causes damping. The spin-transfer torque $d\vec{M}_{\text{STT}}/dt$ can point along the Gilbert damping $d\vec{M}_D/dt$ (green) or opposite to it (red). In the latter case it can destabilize \vec{M} and induce switching or microwave oscillations

After having developed a physical picture for the origin of spin-transfer torques on a quantum-

mechanical level, we now address the question how this torque influences the dynamics of the macroscopically observable magnetization. In order to do so, we have to consider the Gilbert equation,

$$\frac{d\vec{m}}{dt} = \underbrace{-\gamma\vec{m} \times \vec{H}_{\text{eff}}}_{\propto \frac{d\vec{M}_P}{dt}} + \underbrace{\alpha\vec{m} \times \frac{d\vec{m}}{dt}}_{\propto \frac{d\vec{M}_D}{dt}}, \quad (11)$$

which is the equation of motion for a magnetization \vec{m} in an effective field \vec{H}_{eff} . Here, $\vec{m} = \vec{M}/M_S$ is the reduced magnetization, γ the gyromagnetic ratio, and α the phenomenological Gilbert damping constant. The effective field is the negative variational derivative of the total areal energy density E_{tot} comprising contributions from exchange, anisotropy, stray field, and Zeeman energy with respect to the magnetization \vec{M} . The first term in Eq. (11) describes the precessional motion of \vec{m} about \vec{H}_{eff} and the second term the damping, which forces \vec{m} to relax to the lowest energy configuration, $\vec{m} \parallel \vec{H}_{\text{eff}}$ (grey arrows in Fig. 18). Slonczewski [27] expressed the current-induced STT $d\vec{M}_{\text{free}}/dt$ acting on the free layer as

$$\frac{1}{M_S} \frac{d\vec{M}_{\text{free}}}{dt} = \frac{d\vec{m}_{\text{free}}}{dt} = \frac{I}{A} \cdot g(\theta) \cdot \vec{m}_{\text{free}} \times (\vec{m}_{\text{free}} \times \vec{m}_{\text{fixed}}), \quad (12)$$

where I/A is the current density, $g(\theta)$ is the material-dependent STT efficiency function, which is a measure for the conversion of current into STT. In general, it depends on the angle θ between \vec{M}_{free} and \vec{M}_{fixed} . The materials enter into $g(\theta)$ via the spin polarization P , volume and interface resistances, and other transport properties. The double cross product is indeed proportional to $\sin(\theta)$ and, thus, the absorbed transversal component of the spin current as discussed in the context of Fig. 16(a). The linear dependence on I yields the reversed torque upon reversing the current direction. The direction of $d\vec{M}_{\text{free}}/dt$ for the two current polarities is shown in Fig. 18 by the red and green arrows, respectively. In order to study the influence of the STT [Eq. (12)] on the magnetization dynamics it must be included in the Gilbert equation [Eq. (11)] as an additional torque term. After some rearrangement the extended Gilbert takes the form

$$\frac{1}{\gamma} \frac{d\vec{m}}{dt} = \underbrace{-\beta\vec{m} \times \left[\vec{H}_{\text{eff}} + \alpha \frac{I \cdot g(\theta)}{A\gamma} \vec{m}_{\text{fixed}} \right]}_{\text{precession}} - \underbrace{\beta\vec{m} \times \left[\vec{m} \times \left(\alpha\vec{H}_{\text{eff}} - \frac{I \cdot g(\theta)}{A\gamma} \vec{m}_{\text{fixed}} \right) \right]}_{\text{damping/excitation}} \quad (13)$$

with

$$\beta = \frac{1}{1 - \alpha^2}. \quad (14)$$

The subscript *free* is dropped for clarity. The damping constant α is much smaller than unity and, thus $\beta \approx 1$. Due to the smallness of α the impact of the STT on the precessional term, i.e. the precession frequency, in the first term of Eq. (13) is only weak. This component of the STT is called the field-like or perpendicular STT, because it acts like the effective field and points perpendicular to the plane spanned by \vec{M}_{free} and \vec{M}_{fixed} . A second, stronger component of the STT appears in the damping term, where it "competes" with $\alpha\vec{H}_{\text{eff}}$, which is of the same order of magnitude. This component of the STT is called the damping or in-plane STT. Depending on the sign of I the damping due to the STT can be negative or positive, see Fig. 18. The latter case is more interesting, because the conventional damping torque $d\vec{M}_D/dt$ may be compensated or even overcome by the STT term $d\vec{M}_{\text{STT}}/dt$. In this case the precession amplitude increases and \vec{M}_{free} is destabilized, which leads to switching or the excitation of steady-state oscillatory modes.

4.4. Steady-state Oscillatory Modes and Spin-torque Oscillators

In the phenomenological description of current-induced magnetization switching, we have considered the STT and damping terms of the Gilbert equation, but neglected the precessional term. A more complete analysis taking all terms into account shows that the switching process after applying a DC current of the correct polarity starts with the excitation of a precessional motion about the initial state. The cone angle of the trajectory increases steadily under the action of the STT, which opposes the restoring Gilbert torque. When \vec{M} reaches the position, where a potential maximum separates the initial and the final states, switching occurs and \vec{M} relaxes towards the final state, now on a precessional trajectory with decreasing cone angle.

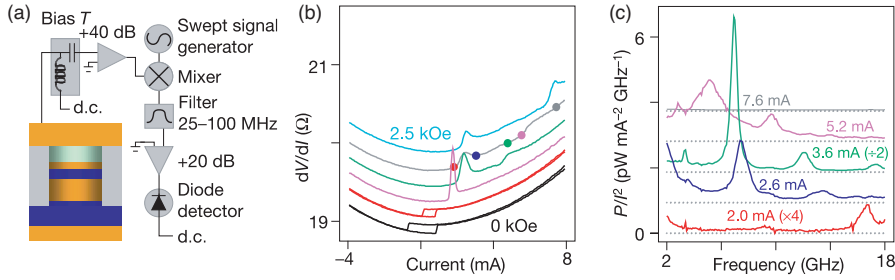


Fig. 19. (a) Experimental setup for the measurement of the microwave signals generated by STT in the nanopillar shown on the left side. (b) Differential resistance versus current for different fields. The hysteresis in the black and red curves vanishes for external fields exceeding the coercivity. Peaks appear instead. (c) Microwave spectra measured at 2 kOe [grey curve in (b)] at different current amplitudes as marked by colored dots in (b). After Ref. [31]

This process only happens if the external field is lower than the coercive field of the free layer. The shape or magnetocrystalline anisotropy then gives rise to at least two stable states, and the current-induced STT can cause switching between them. If the external field exceeds the coercivity only one stable magnetization state exists, namely parallel to the external field, and switching is not possible for either current polarity. For one polarity the system is not excited at all, whereas for the other polarity it enters a steady-state oscillatory motion, which is characterized by equilibrium between $d\vec{M}_D/dt$ and $d\vec{M}_{STT}/dt$, i.e. vanishing of the second term in Eq. (13). In this way, \vec{M}_{free} can be driven into new types of oscillatory dynamic modes, which are not attainable with magnetic fields alone. An example is the large-angle precessional mode with excitation angles as large as 180° is shown in the inset of Fig. 20(b). Any oscillatory motion of the free layer with respect to the fixed layer results, due to the GMR effect, in a variation of the resistance. Therefore, the DC current generates a time-varying voltage with typical frequencies in the GHz range. These signals can be measured with a HF spectrum analyzer setup as shown in Fig. 19(a). Resistance versus current plots similar to Fig. 15(b) for different external fields are shown in Fig. 19(b). With increasing field (from bottom to top) the hysteretic behavior (black and red) gives way for peaks, because external fields larger than 1 kOe (purple curve) exceed the coercivity of the free layer. Microwave spectra taken under the current and field conditions marked in Fig. 19(b) by colored dots are displayed in Fig. 19(c). Rather sharp peaks at frequencies of several GHz are resolved. Figure 20(a) shows the dynamic stability diagram determined from such spectra. The basic features can be reproduced by numerically solving the extended Gilbert equation [Eq. (13)] for a macrospin \vec{M} , which is assumed to represent the be-

havior of the complete magnetization of the free layer. Obviously, the macrospin approximation

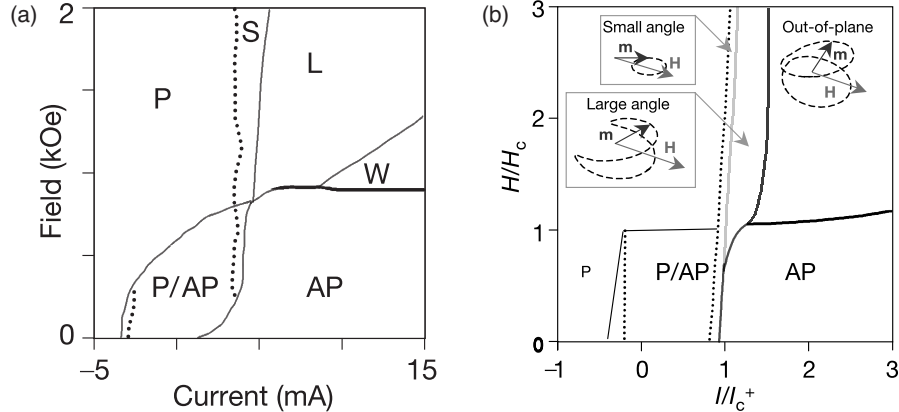


Fig. 20. (a) Experimental and (b) calculated dynamic stability diagram. Different regions are explained in the text. Current and field axes in (b) are normalized to the critical current I_c^+ and the coercive field H_c , respectively. Insets show representative trajectories of steady-state oscillatory modes. After Ref. [31]

is a rather crude one as it neglects all internal magnetic degrees of freedom, e.g. spinwaves. As a consequence only homogeneously magnetized objects can be described. In the diagram, P and AP stand for stable parallel and antiparallel alignment, and P/AP is the region of bistability, where hysteretic switching is possible. S marks the small-amplitude precessional regime and L the large-amplitude dynamic regime. Region W in Fig. 20(a) cannot be described by a macrospin simulation. Micromagnetic simulations have identified region W to correspond to the formation and annihilation of dynamic vortices through the interplay of the current-induced Oersted field and the STT effect [32]. In micromagnetic simulations the object to be described is geometrically subdivided into small volume elements with a size smaller than the exchange length of the material (typically a few nm), within which the assumption of constant magnetization is justified. The Gilbert equation [Eq. (13)] is solved for each element, whereby direct exchange with neighboring volume elements and the demagnetizing field due to all other elements are taken into account via contributions to the effective field. The resulting set of coupled equations is solved by means of finite-element computer codes. Obviously, micromagnetic simulations allow for a much more detailed description of dynamic processes than the macrospin approximation. The accordingly derived stability diagrams (e.g. Fig. 20) show the richness of the highly non-linear current-driven magnetization dynamics. Nanomagnets driven by spin-polarized currents have the potential to serve as nanoscale, on-chip microwave sources or oscillators, tunable by field and current over a wide frequency range. These devices are called spin-torque oscillators (STO). At present the major drawback of STOs is the low output power level of the order of 1 nW. An obvious route to increase the output power is to take advantage of the much larger magnetoresistive effects in, e.g. Fe/MgO/Fe based TMR structures (see Sect. 3.), which exceed typical GMR ratios by about two orders of magnitude. Since STOs are operated under constant-current conditions, the output power scales accordingly. Another route to increase the output of STOs is to operate a large number of them in a synchronized mode. Due to the coherent generation of the microwave signal, one expects that N coupled STOs yield about an N^2 -fold power output. The coupling of STOs can be achieved via spinwaves in a common ferromagnetic layer [33] or via microwave

cross-talk in contact leads [34].

5. Conclusion

We have presented an overview of magnetic and magnetotransport phenomena in layered structures involving magnetic layers: interlayer exchange coupling, GMR, TMR, and current-induced magnetization dynamics. For each effect we first presented a phenomenological description and then developed a physical picture with emphasis on the basic mechanism. All effects only occur at interfaces or for thin enough films, which also require the presence of interfaces. Therefore, layering of magnetic and non-magnetic materials provides new materials with new properties. The discussed effects are nowadays summarized by the term spintronics as they are used to build new electronic devices, which — in addition to the charge of an electron — use its spin to control electronic transport properties. Apart from featuring interesting basic research, spintronics has a high potential for applications mainly in data storage technology. First ideas for a Magnetic Random Access Memory (MRAM) based on Permalloy films dates back to 1955. Since the 1970s thin magnetic films play an important role in harddisk technology as storage media as well as in the read and write-heads. The new phenomena described in this review fit nicely into this tradition: The application of the GMR effect in read-heads of harddisk drives (HHD) was realized only 10 years after its discovery and allowed a significant increase of the storage density. Modern GMR read-heads have sub-micron sized in all three dimensions and, thus, represent a major application of nanotechnology in a multi-billion dollar mass market. Antiferromagnetically coupled (AFC) harddisk media using IEC to increase the thermal stability of the magnetic bits led to a further increase of the storage density. Modern MRAMs employing the TMR effect and an STT based writing scheme can now be realized as highly integrated solid state devices. They have the potential to replace semiconductor-based memories (DRAMs) because of their nonvolatility, the lower energy consumption, and the higher scalability. A new magnetic storage concept called Magnetic Racetrack Memory [35] employs STT effects to move magnetic domain walls, which carry the stored information, along a magnetic wire. Spin-torque oscillators play a crucial role for the microwave-assisted writing scheme of future write-heads and are also envisaged for applications in communication technology, e.g. for inter- and intrachip communication. Angle and position sensors based on GMR, e.g. for applications in the automotive industry, are available already since 1996. Further applications in magnetocouplers, strain sensors, reprogrammable logic devices, and biochips [36] are in development.

References

- [1] Reviews: D.E. Bürgler, P. Grünberg, S.O. Demokritov, M. T. Johnson, in *Handbook of Magnetic Materials*, **13**(2001) ed. by K.H. J. Buschow, Elsevier; P. Grünberg, D. Pierce, in *Encyclopedia of Materials: Science and Technology*, Elsevier, 2001.
- [2] S.S. Yan, R. Schreiber, F. Voges, C. Osthöver, P. Grünberg, *Phys. Rev. B*, **59**(1999), 11641.
- [3] J.C. Slonczewski, *J. Magn. Magn. Mater.*, **150**(1995), 13.
- [4] M. Stiles, Private communication.
- [5] Q. Leng, V. Cros, R. Schäfer, A. Fuss, P. Grünberg, W. Zinn, *J. Magn. Magn. Mater.*, **126**(1993), 367.

- [6] J. Mathon, M. Villeret, D.M. Edwards, R.B. Muniz, *J. Magn. Magn. Mater.*, **121**(1993), 242; P. Bruno, *Phys. Rev. B*, **52**(1995), 411; M. Stiles, *J. Magn. Magn. Mater.*, **200**(1999), 322.
- [7] Reviews: P.M. Levy, *Solid State Phys.*, **47**(1994), 367; A. Fert, P. Grünberg, A. Barthélémy, F. Petroff, W. Zinn, *J. Magn. Magn. Mater.*, **140-144**(1995), 1; A. Barthélémy, A. Fert, F. Petroff, in *Handbook of Magnetic Materials*, **12**(1999) ed. by K.H.J. Buschow, Elsevier; A. Fert, in *Encyclopedia of Materials: Science and Technology*, Elsevier (2001); M.A.M. Gijs, G.E.W. Bauer, *Adv. Phys.*, **46**(1997), 285.
- [8] M.N. Baibich, J.M. Broto, A. Fert, F.N.V. Dau, F. Petroff, P. Etienne, G. Creuzet, A. Friedrich, J. Chazelas, *Phys. Rev. Lett.* **61**(1988), 2472.
- [9] G. Binasch, P. Grünberg, F. Saurenbach, W. Zinn, *Phys. Rev. B*, **39**(1989), 4828.
- [10] D. Dieny, *J. Magn. Magn. Mater.*, **136**(1994), 335.
- [11] P.A. Grünberg, *Sensors and Actuators A*, **91**(2001), 153.
- [12] J. Barnaś, A. Fuss, R.E. Camley, P. Grünberg, W. Zinn, *Phys. Rev. B*, **42**(1990), 8110.
- [13] http://www.fz-juelich.de/iff/D_Buergler_gmr/
- [14] M. Jullière, *Phys. Lett.*, **54A**(1975), 225.
- [15] T. Miyazaki, N. Tezuka, *J. Magn. Magn. Mater.*, **139**(1995), L231.
- [16] J.S. Moodera, L.R. Kinder, T.M. Wong, R. Meservey, *Phys. Rev. Lett.*, **74**(1995), 3273.
- [17] Review: J. Moodera, G. Mathon, *J. Magn. Magn. Mater.*, **200**(1999), 248.
- [18] X.-F. Han, T. Daibou, M. Kamijo, K. Yaoita, H. Kubota, Y. Ando, T. Miyazaki, *Jpn. J. Appl. Phys.*, **39**(2000), L439.
- [19] D. Wang, C. Nordman, J.M. Daughton, Z. Qian, J. Fink, *IEEE Trans. Magn.*, **40**(2004), 2269.
- [20] M. Sharma, S.X. Wang, J.H. Nickel, *Phys. Rev. Lett.*, **82**(1999), 616.
- [21] J.M. De Teresa, A. Barthélémy, A. Fert, J.P. Contour, F. Montaigne, P. Seneor, *Science*, **286**(1999), 507.
- [22] W.H. Butler, X.G. Zhang, T.C. Schulthess, J.M. MacLaren, *Phys. Rev. B*, **63**(2001), 054416.
- [23] S. Yuasa, T. Nagahama, A. Fukushima, Y. Suzuki, K. Ando, *Nature Materials*, **3**(2004), 868.
- [24] S.S.P. Parkin, C. Kaiser, A. Panchula, P.M. Rice, B. Hughes, M. Samant, S.H. Yang, *Nature Materials*, **3**(2004), 862.
- [25] Y.M. Lee, J. Hayakawa, S. Ikeda, F. Matsukura, H. Ohno, *Appl. Phys. Lett.*, **90**(2007), 212507.
- [26] Reviews: M.D. Stiles, J. Miltat, in *Spin dynamics in confined magnetic structures III*, ed. by B. Hillebrands, A. Thiaville, Topics in Applied Physics, **101**(2006), Springer; J. Slonczewski, in *Handbook of Magnetism and Advanced Magnetic Materials*, ed. by H. Kronmüller, S.S.P. Parkin, Spintronics and Magnetoelectronics, Wiley, **5**(2007).

- [27] J.C. Slonczewski, *J. Magn. Magn. Mater.*, **159**(1996), L1.
- [28] L. Berger, *Phys. Rev. B*, **54**(1996), 9353.
- [29] J.A. Katine, F.J. Albert, R.A. Buhrman, E.B. Myers, D.C. Ralph, *Phys. Rev. Lett.*, **84**(2000), 3149.
- [30] M.D. Stiles, A. Zangwill, *Phys. Rev. B*, **66**(2002), 014407.
- [31] S.I. Kiselev, J.C. Sankey, I.N. Krivorotov, N.E. Emley, R.J. Schoelkopf, R.A. Buhrman, D.C. Ralph, *Nature*, **425**(2003), 380.
- [32] K.J. Lee, A. Deac, O. Redon, J.P. Nozières, B. Dieny, *Nature Materials*, **3**(2004), 877.
- [33] S. Kaka, M. Pufall, W.H. Rippard, T.J. Silva, S.E. Russek, J. Katine, *Nature*, **437**(2005), 389.
- [34] J. Grollier, V. Cros, A. Fert, *Phys. Rev. B*, **73**(2006), 060409.
- [35] S.S.P. Parkin, M. Hayashi, L. Thomas, *Science*, **320**(2008), 190.
- [36] M.M. Miller, P.E. Sheehan, R.L. Edelstein, C.R. Tamanaha, L. Zhong, S. Bounnak, L.J. Whitman, R.J. Colton, *J. Magn. Magn. Mater.*, **225**(2001), 138.

Спинтроника: магнетизм и спин-зависящий транспорт на нанометровом масштабе

Даниел Е. Бёрглер

С момента открытия межслойного обмена и эффекта гигантского магнитосопротивления (ГМС) в начале 1980-х спин-зависящий транспорт в магнитных нанослоях и наноструктурах привлекает большое внимание. Исследования мотивируются применениями ГМС считывающих головок в компьютерных жестких дисках и памяти, а также новыми открытиями в области, называемой сейчас спинтроника. Эта область быстро развивается в направлении нанотехнологии, использующей магнетизм и спин-зависящий транспорт на нанометровом масштабе. Спинтроника получила признание присуждением Нобелевской премии 2007 г. за открытие ГМС эффекта. В настоящем обзоре обсуждаются также дальнейшие современные открытия в спинтронике.

Ключевые слова: спинтроника, наноструктуры, нанотехнологии, гигантское магнитосопротивление.